XIX IMEKO World Congress
Fundamental and Applied Metrology
September 6–11, 2009, Lisbon, Portugal

NEW NON-DESTRUCTIVE TEST TECHNIQUE ON METAL INSPECTION

L. Rosado [1], T. Santos [2], M. Piedade [3], Pedro M. Ramos [4], P. Vilaça [5]

[1,3] IST, UTL, Lisbon, Portugal, luis.rosado@ist.utl.pt, msp@inesc-id.pt
[2,5] IDMEC, DEM, IST, UTL, Lisbon, Portugal, telmo.santos@ist.utl.pt, pedro.vilaca@ist.utl.pt
[4] Instituto de Telecomunicações, DEEC, IST, UTL, Lisbon, Portugal, pedro.ramos@lx.it.pt

Abstract − In this paper a new non-destructive testing (NDT) system focusing on micro size superficial defects in metals is presented. The innovative system is composed by a new type of eddy currents probe, electronic devices for signal generation, conditioning and conversion, automated mechanized scanning and analysis software. The key original aspect of this system is the new type of eddy currents probe. This new IOnic probe provides enhanced lift-off immunity and improved sensitivity for micro size imperfections. The probe concept was studied using a Finite Element Modeling (FEM) tool and experimental verified using a standard defect.

The testing results on some Friction Stir Welding (FSW) specimens clearly show that the system is able to detect cracks about 50 μm depth, which significantly increases the actual state of the art in NDT reliability for micro imperfections detection. The system can be applied to a broad range of industries which include manufacturing, maintenance and engineering companies.

Keywords: Eddy currents probe; Non-destructive testing; Friction Stir Welding.

1. INTRODUCTION

The localization and micro structural characterization of some material imperfections lead to large difficulties when using conventional or even advanced NDT techniques [1][2]. An industrial example is the superficial micro-cracks of less than 60 μm, common on FSW [3]. In fact, the quality assessment of FSW presents a paradigm in NDT, because these defects are characterized by no physical material discontinuities with a very low size and low energy reflection effect [4]. Furthermore there are conductivity changes due to the FSW process itself, making the detection of defects difficult [5][6].

In order to overcome these problems and increase the defects detection on such application, a new type of eddy currents probe was specially designed and patented [7]. To validate the IOnic probe concept, a measuring system was designed and manufactured. The testing results on some Friction Stir Welding (FSW) specimens clearly show that the system is able to detect cracks about 50 μm depth, which significantly increases the actual state of the art in NDT reliability for micro imperfections detection.

2. NEW TYPE OF EDDY CURRENTS PROBE

The main innovative aspect of the system is the entirely new design of the IOnic eddy current probe. IOnic probe morphology exhibits a driver/pickup arrangement and at the same time, a differential based operation. The driver element is a copper trace placed in the middle of two pickup planar coils wired on opposite directions as is shown in Fig. 1.

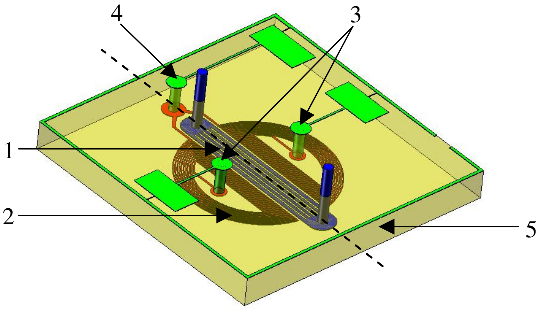

Fig. 1. Tri-dimensional view of IOnic probe.
1) Driver trace, 2) Pickup coil, 3) Output terminals,
4) Common terminal, 5) Substrate.

When an alternate current $\bar{I}$ is made to flow in the driver trace, the lines of the generated magnetic field are orthogonal and concentric around it. This magnetic field induces eddy currents on the material and at same time is sensed on the pickup coils as electromotive force. By being symmetrical and sharing a common terminal, the pickup coils form a differential magnetic field sensor. In the presence of any perturbation that could modify the symmetry of the magnetic field among the axis on Fig. 1, a voltage signal $\bar{U}_{out}$ is created between the pickup coils output terminals. The defect detection is done by characterizing $\bar{U}_{out} / \bar{I}$ along the test material.

The software CST EM Studio was used to model the probe and to verify the eddy currents disposition inside the test material. Using the elements available in the software package, the probe model shown in Fig. 2 was build. The model was placed in the air and 300 μm above a piece of aluminum. The analysis was performed using a hexahedral mesh of 1.22×10^6 elements with local refinement.

When the magnetic stimuli are created around the driver trace, eddy currents appear in the material as a reaction to oppose this magnetic field. As is shown in Fig. 2 eddy currents describe loops passing underneath the driver trace and circular paths defined through the material. Along the symmetry axis, the induced eddy currents take the opposite direction of the current flowing in the driver trace. On the plot on Fig. 2, a sine wave with 1 A amplitude and frequency of 500 kHz is flowing in the driver trace. Eddy currents are drawn when the phase of the sine wave is equal to 90º.

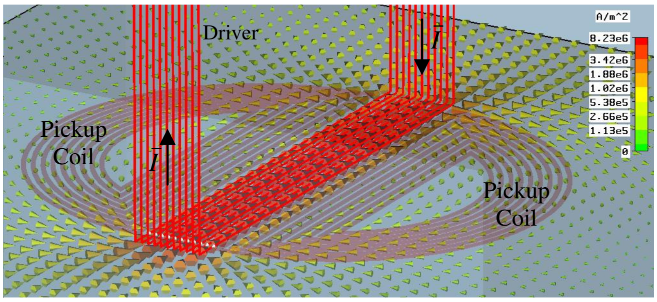

Fig. 2. Probe Model and superficial eddy currents.

Using this model, the value of $\overline{U}_{out}$ can be computed as the difference between the sums of the electromotive force sensed on the spirals that compose each coil.

A standard defect with 10 mm depth and 300 µm width was defined on the aluminum piece. Although the dimensions of this defect are bigger than the dimension of real defects, it was used as a reference to validate the probe concept. The probe was moved on a sweep with 500 µm steps as shown on Fig. 3.

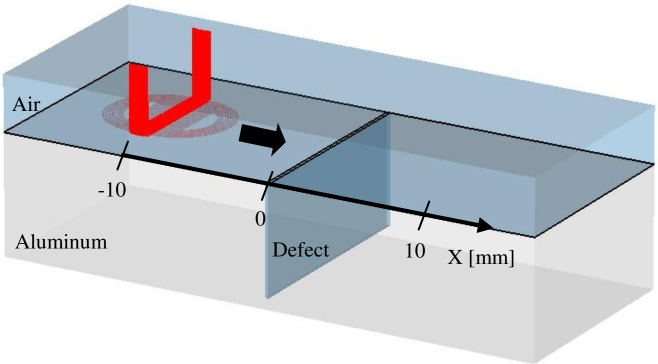

Fig. 3. Defect characterization sweep.

During the sweep, the successive values for $\overline{U}_{out} / \overline{I}$ were registered and plotted on Fig. 4. As expected, when the probe is away from the defect, the induced voltage is roughly zero. When the sensitive coils overlap the defect, the signal output increases returning to zero when the defect is perfectly centered with the probe symmetry axis.

The presence of the defect is clearly shown on both the imaginary and real part of $\overline{U}_{out} / \overline{I}$. However, the defect contribution is principally observed on the imaginary part of $\overline{U}_{out} / \overline{I}$. For a defect like this and similar driver trace current, the maximum excepted output amplitude is about 2.4 mV.

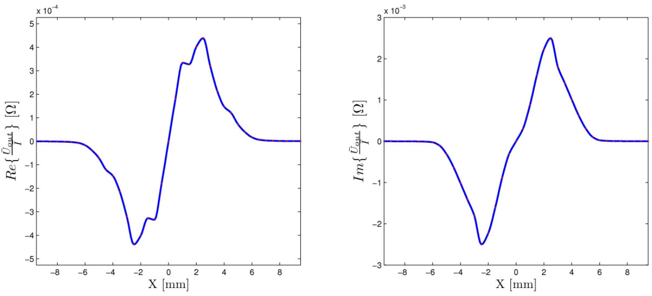

Fig. 4. Real and imaginary part of $\overline{U}_{out} / \overline{I}$ along the sweep.

The IOnic probe has some advantages when compared to the conventional eddy currents probes:

- Differential based operation resulting on high sensibility and superior lift-off immunity.
- Improved contact with test material by being planar, leading to deeper eddy currents penetration in test material.
- The straight eddy currents induced in the material near the driver trace can be taken as advantage to evaluate materials where the flaws tend to follow a specific orientation.
- Allow the inspection of the material borders as long as the symmetry axis remains perpendicular to it.
- It can be used on non-planar and complex geometry surfaces.
- Despite the preferred operation mode is the differential, the probe can also perform absolute measurements. This will provide information on material parameters such as conductivity, magnetic permeability and thickness.

3. MEASUREMENT SYSTEM

The system assembly is shown in Fig. 5 and individual components are described along this section. Despite the possibility to directly acquire $\overline{U}_{out}$ signal with the DAQ, this approach limits the possible frequency range for the system operation. To avoid this, the amplitude and phase detection was done using analog and mixed-signals circuits.

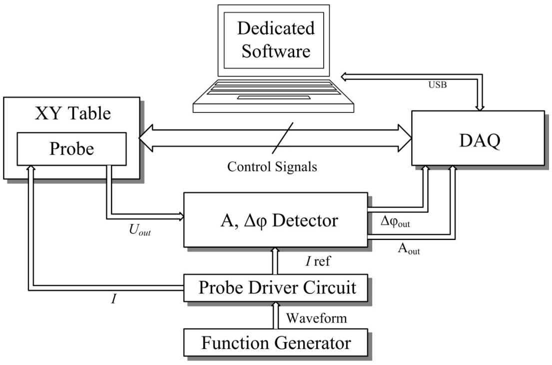

Fig. 5. System overview.

The amplitude and phase difference detector and the probe driver circuits have been assembled on a metallic chassis as is shown in Fig. 6. The circuits are powered by a 12 V power supply.

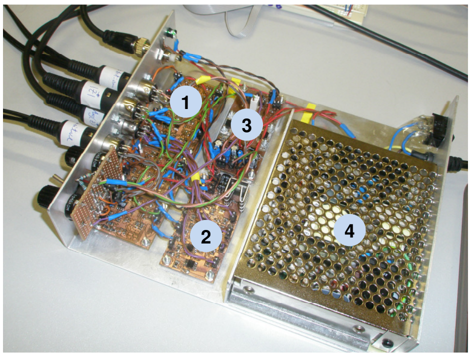

Fig. 6. Analog and mixed-signals circuits. 1) Amplitude detector, 2) Phase detector, 3) Probe driver circuit, 4) Power supply.

3.1. IOnic Probe

The probe was manufactured on 1.6 mm dual layer FR4 PCB substrate (Fig. 7). The driver trace has 10 mm length and 1.5 mm width. The two sensitive coils are formed by seven turns made with tracks of 100 μm width separated by same dimension gaps.

The dimensions used to build this probe were the same used on the FEM analysis. This will allow comparing the simulation and the experimental results.

Fig. 7. Manufactured IOnic probe.

3.2. XY Table

To enable the system to move the probe along the test material a XY table was used. The constructed device has a resolution of 125 μm and is controlled by stepper motors attached to the digital ports of the DAQ.

3.3. DAQ

The signals processed on the amplitude and phase detector are acquired using a 16-bit DAQ from National Instruments (NI USB-6251) and transferred to the personal computer via USB.

3.4. Probe Driver Circuit

As the IOnic probe needs a substantial current on the excitation filament to create the necessary excitation magnetic field, a current buffer was designed using a general purpose OPAMP. The circuit has a transconductance gain of 1 A.V^{-1} and is controlled by the signal from the function generator (Fig. 8). The maximum output current was set to 1.1 A and the operation frequency range from 10 kHz to 1 MHz.

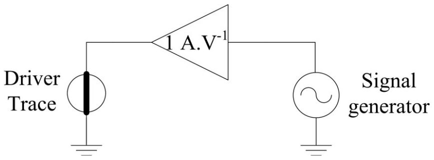

Fig. 8. Probe driver.

3.5. Amplitude and phase difference detector

This block is responsible for generating DC signals proportional to the amplitude of the probe output signal and the phase difference between this signal and the driver trace current reference. As seen before, even with an extreme defect and with a 1 A amplitude sine wave flowing on the driver trace, the excepted probe output signal has only about 2.4 mV. Because of this reason, the first stage of this circuit is a 40 dB voltage amplifier created using an high speed OPAMP (Fig. 9). After being amplified, the signal is processed by an RMS-DC converter. As the RMS-DC gain is 7.5V/V$_{\mathrm{RMS}}$, the output of the amplitude detector is

$$A_{out} = \frac{7.5}{\sqrt{2}} \times 100 \times A(\overline{U}_{out}) \qquad (1)$$

where $A(\overline{U}_{out})$ is the amplitude of the pickup coil signal.

The phase difference is computed by digitalizing both the signals with a comparator and executing the XOR binary operation to generate a signal whose average value is proportional to the phase difference between the input signals. To obtain the average value, a RC low pass filter with a cut-off frequency of 100 Hz was used. As the XOR operation is performed with 5 V digital logic, the output of the phase difference detector is

$$\Delta\varphi_{out} = 5 \times \Delta\varphi(\overline{U}_{out}, \bar{I}_{ref}), \qquad (2)$$

where $\Delta\varphi(\overline{U}_{out}, \bar{I}_{ref})$ is the phase difference between the probe output signal and the driver trace current reference.

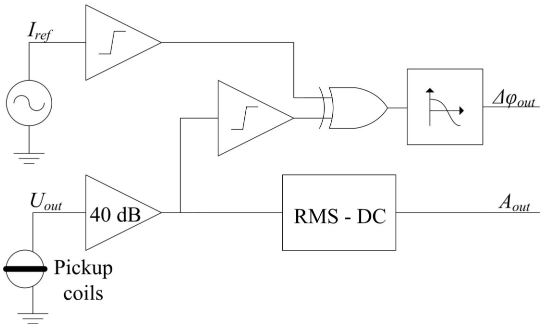

Fig. 9. Amplitude and phase detector.

3.6. Dedicated software

Analysis software was developed on LabVIEW and allows to process, monitoring and save the acquired signals in real-time and to control the XY table. A post processing feature was added to localize and characterize the detected defects.

4. EXPERIMENTAL RESULTS

The defect studied on the FEM analysis was reproduced by electro-erosion on a piece of aluminum. The system was used to perform the sweep described on Fig. 3. As in the FEM analysis, the driver trace current is a sine wave with 500 kHz frequency and 1 A amplitude. The results for both FEM and experimental sweeps are registered in Fig. 10.

It can be seen that there is a good similarity between the two results, principally on the imaginary part of the output signal. The main differences between the two curves are observed on the real part.

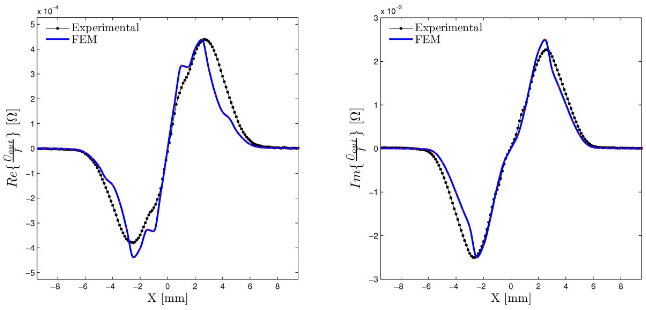

Fig. 10 - Experimental and FEM results for the standard defect.

To evaluate the system performance, some FSW specimens where inspected. FSW is a solid-state joining process patented in 1991. There is a huge potential on using this technology and it is considered the main advance on joining technology during the last decade. FSW is performed without any filler material or gas protection and at lower temperatures than the fusion temperature of the involved materials, leading to low level of joint distortion and residual tension. In FSW, a non-consumable cylindrical tool is rotated at a constant speed through a joint line involving the work pieces to be joined which are overlapped or butted together as is shown in Fig. 11.

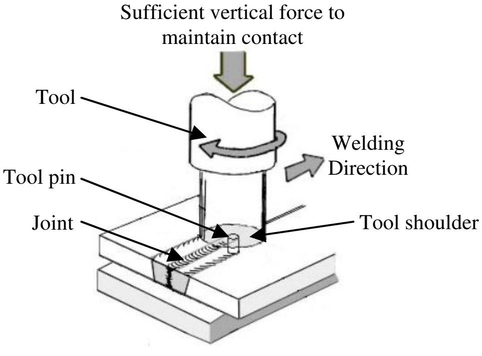

Fig. 11. FSW Process.

Frictional heat is generated both internally by viscous dissipation and at the interfaces between the tool pin and shoulder and the material of the work pieces. This heat causes the materials to soften without reaching the melting point, entering the viscous-plastic domain. As the tool is moved in the welding direction, the leading face of the tool forces plasticized material to flow back mainly around the retreating side while applying a substantial force to consolidate the weld. There are several welding parameters taking influence over the final welding quality, namely: vertical force, rotation speed, travel speed, tool geometry and tilt angle between the tool and welding materials. The right choice and application of the welding parameters will result on sound welds. Nevertheless, under industrial production environment some defects may arise. Defects on FSW are very different from fusion weld typical defects and can have different origins, morphology and size. Beside these defects, there are conductivity modifications due to metallurgical changes as the dynamical recristalization and recovering for the aluminum alloys.

FSW has been applied in a broad range of applications like shipbuilding, aerospace, railway and others. However, FSW consolidation requires reliable NDT techniques and procedures which the actual state of the art does not enable. Actually, the commercially available NDT techniques do not allow detecting important FSW defects with influence over the structural performance of the welded construction.

A set of joints were produced in aluminum alloy AA2024-T531 with thickness of 3.8 mm. The welding parameters were chosen in order to produce three distinct types of root defects (Fig. 12). Results were measured along a sweep on the perpendicular direction of the joint, with the driver trace parallel to it. The starting point of the test is set to 25 mm before the joint and 50 mm long segments are characterized with 250 μm distance between each acquisition. In all the acquisitions, the real and imaginary part of $\bar{U}_{out}/\bar{I}$ are measured at 50, 100, 250 and 750 kHz. The imaginary part of $\bar{U}_{out}/\bar{I}$ for the three types of defects for three of those frequencies is shown in Fig. 13.

As FSW process causes material conductivity changes, even in non-defective conditions, the joint is responsible for the large curve on the processed imaginary part. The presence of defects creates a small perturbation observed on the middle of the joint, highlighted in red on Fig. 13. The different types of defects can be detected and there is a very good proportionality between the defect dimension and the observed perturbation on the imaginary part of $\bar{U}_{out}/\bar{I}$.

The quantification of the detected defects is done by finding the maximum, $(x_2, \bar{S}(x_2))$ and the minimum $(x_1, \bar{S}(x_1))$ values for $\bar{S}(x) = Im(\bar{U}_{out}/\bar{I})$, then compute

$$r(x) = \frac{\bar{S}(x_2) - \bar{S}(x_1)}{x_2 - x_1} x + \bar{S}(x_1) - \frac{\bar{S}(x_2) - \bar{S}(x_1)}{x_2 - x_1} x_1 \qquad (3)$$

and finally the defect index

$$DI = \int_{x_1}^{x_2} \left| \bar{S}(x) - r(x) \right| dx \,. \qquad (4)$$

The defect level is a integral measurement of the verified perturbation comparatively to the segment line containing the maximum and the minimum of $\bar{S}(x)$. The chosen way to quantify the defects was by computing the area defined by the difference between $\bar{S}$ and r. The defect index is a characteristic variable of $\bar{S}$ which numerically demonstrate an important aspect of their behavior correlated with the defects presence.

The application of the defect index is illustrated in Fig. 14 for the defect type 0 and II. In defect type 0, the segment line r is close the $\bar{S}$ leading to a small value of DI on the other side, on the defect of type II, the perturbation leads to a higher defect level.

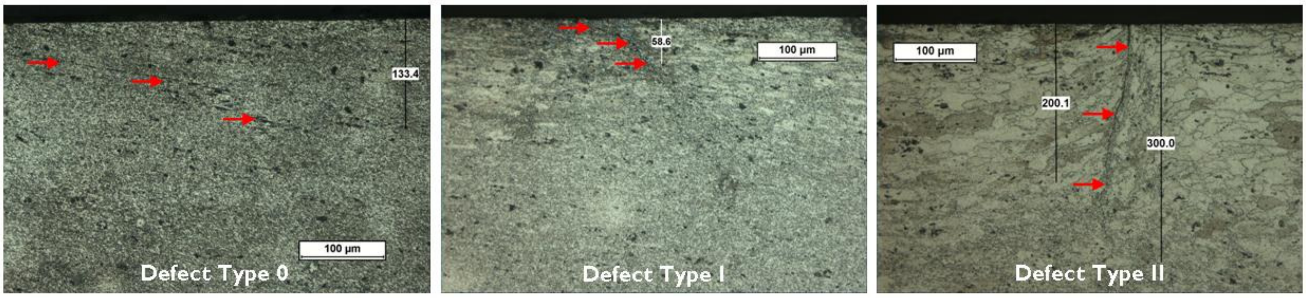

Fig. 12. Transversal macrographs of three different FSW defective joints.
Defect Type 0: oxides alignment, Defect Type I: ≈60 µm, Defect Type II: ≈200 µm.

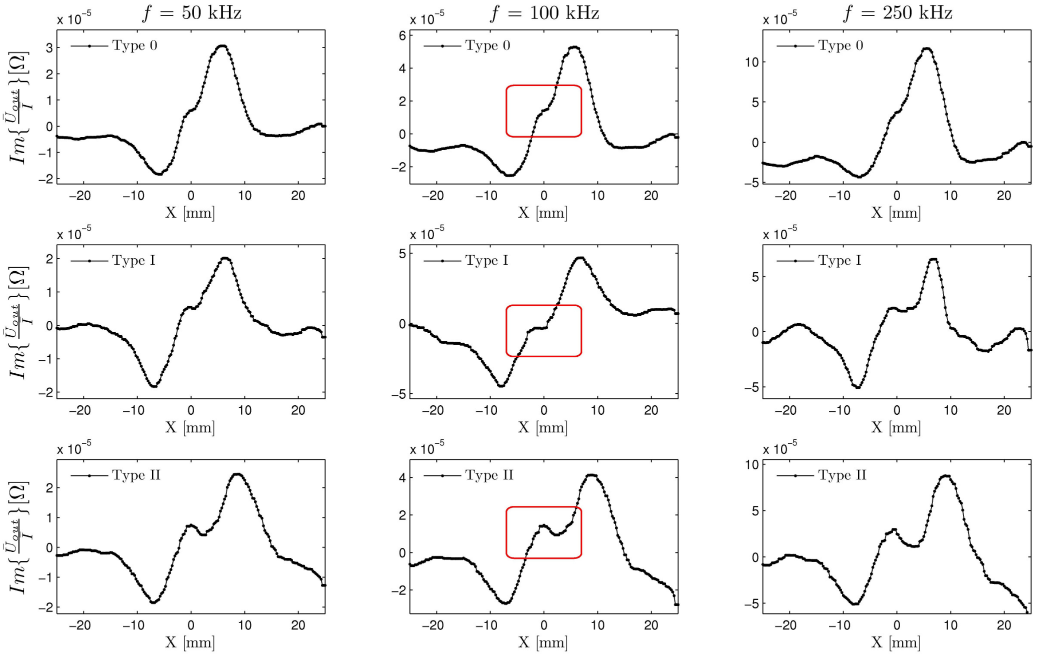

Fig. 13. Results for the FSW joints with defect types 0, I and II for 50, 100 and 250 kHz frequencies.

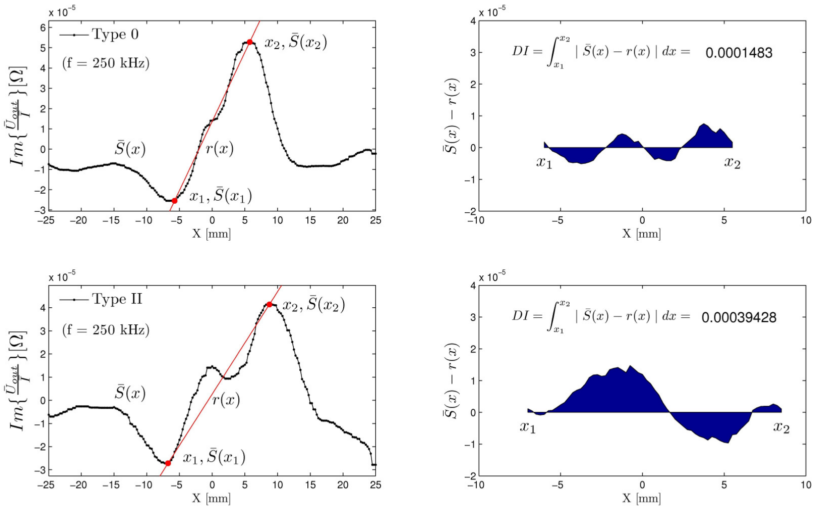

Fig. 14. Graphical meaning of defect index.

The defect level for the different defects are shown in Fig. 15, which demonstrates a good test coherency as the results have the same behavior at different frequencies.

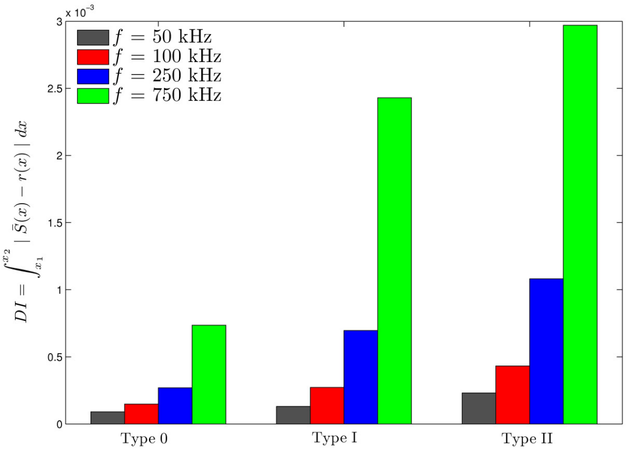

Fig. 15. Defect index for the three FSW joints and test frequencies.

5. CONCLUSIONS

The operation of the IOnic probe is based on a integration effect along each turn of the sensitive coils and, at the same time, on a differential operation between the two coils. With the IOnic probe is possible to identify a distinctive characteristic on the output signals in presence of defects which is very easy to interpret. The verified characteristic is proportional to the dimension of the three tested defects in all the frequencies used. Numerical quantification through the algorithm presented allows deducing the relative dimension between the defects.

Unlike conventional probes, which are based on the absolute value of the real and imaginary part of the signal, the defect identification on IOnic probe is based on a relative change of the output signal. This fact makes the new probe less dependent to unwanted interferences such as probe lift-off, material magnetic permeability and conductivity changes and also electronic issues.

Based on the presented results, this approach leads to a very sensitive and also effective probe able to detect micro size defects.

ACKNOWLEDGMENTS

The authors would like to acknowledge Fundação para a Ciência e a Tecnologia (FCT) and FEDER for its financial support via: projects PTDC/EME-TME/69999/2006 and PTDC/EEA-ELC/72875/2006 and the PhD scholarship FCT- SFRH/BD/29004/2006.

REFERENCES

[1] S. Iwaki, T. Okada, N. Eguchi, S. Tanaka, K. Namba, N. Oiwa, “Imperfections in friction stir welded zones and their precision non-destructive testing. Studies on characteristics of friction stir welded joints in structural thin aluminium alloys”, *Welding International*, vol. 20, n. 3, pp. 197-205, 2006.

[2] G. Dobmann, “Non-destructive microstructure characterization of material states after thermal ageing, fatigue loads, and neutron irradiation”, *61st Annual Conference of the IIW*, Graz, Austria, 6 – 11 July 2008.

[3] International patent Nº PCT/GB92/02203, Inventors: W. M. Thomas, December, 1991.

[4] Z. Caizhi, Y. Xinqi, L. Guohong, “Effect of oxide array on the fatigue property of friction stir welds”, *Scripta Materialia*, vol. 54, pp. 1515–1520, 2006.

[5] T. Santos, P. M. Ramos, P. Vilaça, “Non destructive testing of friction stir welding: Comparison of planar eddy current probes”, *IMEKO TC4 Symp*osium, Florence, Italy, pp. 507-512, September, 2008.

[6] D. Grundy, V. Zilberstein, N. Goldfine, “MWM®-Array Inspection for Quality Control of Friction Stir Welded Extrusions”, *ASM 7th International Conference on Trends in Welding Research*, Pine Mountain GA, May 16-20, 2005.

[7] Portuguese Patent N.º PT 104089 – *Método de Ensaio Não Destrutivo Baseado em Variante de Sonda de Correntes induzidas*, Inventors: Telmo Santos, Moisés Piedade, Pedro Vilaça, June, 2008 (in portuguese).